ASTRONOMY

Universal interferometric signatures of a black hole's photon ring

Michael D. Johnson[1,2]*, Alexandru Lupsasca[2,3,4]*, Andrew Strominger[2,3], George N. Wong[5,6], Shahar Hadar[2,3], Daniel Kapec[7], Ramesh Narayan[1,2], Andrew Chael[1,2,8,9], Charles F. Gammie[5,10], Peter Galison[2,3,11], Daniel C. M. Palumbo[1,2], Sheperd S. Doeleman[1,2], Lindy Blackburn[1,2], Maciek Wielgus[1,2], Dominic W. Pesce[1,2], Joseph R. Farah[1,2,12], James M. Moran[1]

The Event Horizon Telescope image of the supermassive black hole in the galaxy M87 is dominated by a bright, unresolved ring. General relativity predicts that embedded within this image lies a thin "photon ring," which is composed of an infinite sequence of self-similar subrings that are indexed by the number of photon orbits around the black hole. The subrings approach the edge of the black hole "shadow," becoming exponentially narrower but weaker with increasing orbit number, with seemingly negligible contributions from high-order subrings. Here, we show that these subrings produce strong and universal signatures on long interferometric baselines. These signatures offer the possibility of precise measurements of black hole mass and spin, as well as tests of general relativity, using only a sparse interferometric array.

INTRODUCTION

The Event Horizon Telescope (EHT) Collaboration has recently published images of the supermassive black hole in M87 using very long baseline interferometry (VLBI) at 1.3-mm wavelength (*1*–*6*). These images reveal a bright ring of emission with a diameter of approximately 40 μas. However, while the diameter of this ring is resolved by the EHT, its thickness and detailed substructure are not. Here, we show that general relativity predicts an intricate substructure in the ring that presents distinctive signatures for interferometric measurements. These signatures offer a promising approach for precisely determining the mass and spin of black holes and for testing general relativity using sparse interferometers, such as an extension of the EHT to space.

Neglecting opacity, a telescope with perfect resolution directed at a black hole observes an infinite number of nested images of the universe. These images arise from photons that differ by the number n of half-orbits that they complete around the black hole on the way from their source to the detector. Each such image is thus an increasingly delayed and demagnified snapshot of the universe as seen from the black hole. In an astrophysical setting, this self-similar sequence of relativistic images is dominated by the luminous matter surrounding the black hole and produces in its image a feature known as the "photon ring" of the black hole (*7*–*10*). The leading ($n = 1$) subring appears as a sharp, bright feature in ray-traced images from many general relativistic magnetohydrodynamic (GRMHD) simulations (see Fig. 1). Successive subrings have exponentially sharper profiles and asymptotically approach the boundary of the black hole "shadow." For large n, these profiles mirror the leading subring in a manner that universally depends on the spacetime geometry, with the ratio of successive subring flux densities determined by Lyapunov exponents that characterize the instability of bound photon orbits. Hence, measuring the size, shape, and thickness of the subrings would provide new and powerful probes of a black hole spacetime.

Both GRMHD simulations and analytic estimates suggest that the photon ring should provide only ~10% of the total image flux density. This dimness may appear to preclude observations of the photon ring and its substructure, which is dimmer still. However, interferometric measurements are sensitive to more than just overall flux: They also natively filter images by their spatial wave numbers and therefore naturally isolate contributions from individual photon subrings. Sufficiently long baselines also resolve out diffuse flux in an image and are thus dominated by power from the photon ring. Hence, although sharp elements of the photon ring produce a negligible contribution to the total flux in an image, they can still provide a pronounced, dominant signal on long baselines.

In this Research Article, we explore the photon ring's theoretical underpinnings and show that, unexpectedly, precise measurements of the photon ring and even its subrings are feasible using interferometry. We describe the shell of bound photon orbits of a Kerr black hole and its relation to the photon ring. We also present a decomposition of the photon ring into subrings indexed by half-orbit number and derive their self-similar structure, which is universally governed by Lyapunov exponents that characterize orbital instability. We then derive generically expected interferometric signatures of the photon ring. We show that its subrings produce a cascade of damped oscillations on progressively longer baselines, with the visibility of each subring conveying precise information about its diameter, width, and angular profile. Last, we discuss observational prospects for detecting these signatures with extensions of the EHT. In particular, we highlight the possibility of detecting the leading $n = 1$ subring using a station in low Earth orbit, the $n = 2$ subring using a station on the Moon, and the $n = 3$ subring using a station in the Sun-Earth L_2 orbit.

[1]Center for Astrophysics | Harvard and Smithsonian, 60 Garden Street, Cambridge, MA 02138, USA. [2]Black Hole Initiative at Harvard University, 20 Garden Street, Cambridge, MA 02138, USA. [3]Department of Physics, Harvard University, Cambridge, MA 02138, USA. [4]Society of Fellows, Harvard University, Cambridge, MA 02138, USA. [5]Department of Physics, University of Illinois, 1110 West Green Street, Urbana, IL 61801, USA. [6]CCS-2, Los Alamos National Laboratory, P.O. Box 1663, Los Alamos, NM 87545, USA. [7]School of Natural Sciences, Institute for Advanced Study, Princeton, NJ 08540, USA. [8]Princeton Center for Theoretical Science, Jadwin Hall, Princeton University, Princeton, NJ 08544, USA. [9]NASA Hubble Fellowship Program, Einstein Fellow. [10]Department of Astronomy, University of Illinois at Urbana-Champaign, 1002 West Green Street, Urbana, IL 61801, USA. [11]Department of History of Science, Harvard University, Cambridge, MA 02138, USA. [12]University of Massachusetts Boston, 100 William T. Morrissey Blvd., Boston, MA 02125, USA.
*Corresponding author. Email: mjohnson@cfa.harvard.edu (M.D.J.); lupsasca@fas.harvard.edu (A.L.)

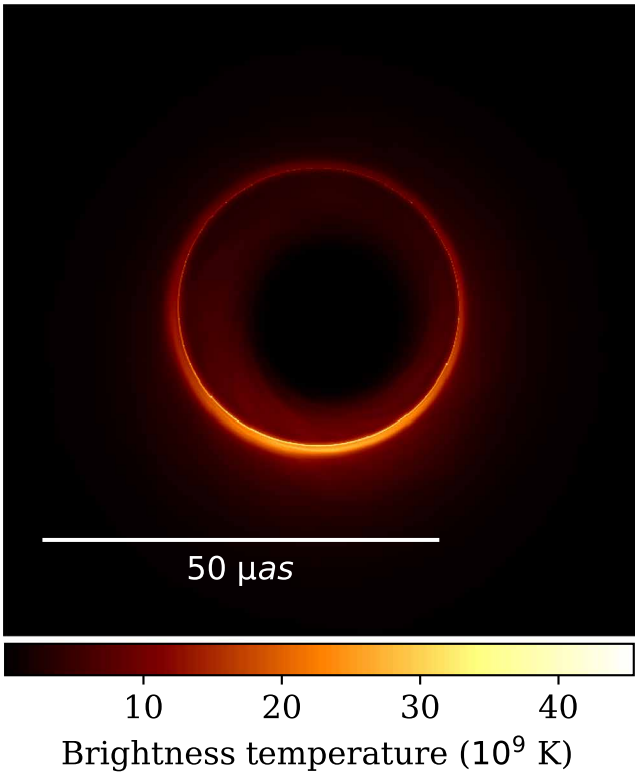

Fig. 1. Time-averaged image of a GRMHD simulation of M87. This model has parameters chosen to be consistent with the 2017 EHT data and corresponds to the high magnetic flux "magnetically arrested disk" accretion state. It has $M = 6.2 \times 10^9 M_\odot$, $a/M = 0.94$, $\theta_{obs} = 163°$, $r_{high} = 10$, and mass accretion rate matching the 1.3-mm flux density (*5*). The spin axis points left when projected onto the image. The time average was performed over 100 snapshots produced from uniformly spaced GRMHD fluid samples over a time range of 1000*M* (approximately 1 year). Although visually prominent, the thin, bright ring contains only ~20% of the total image flux density.

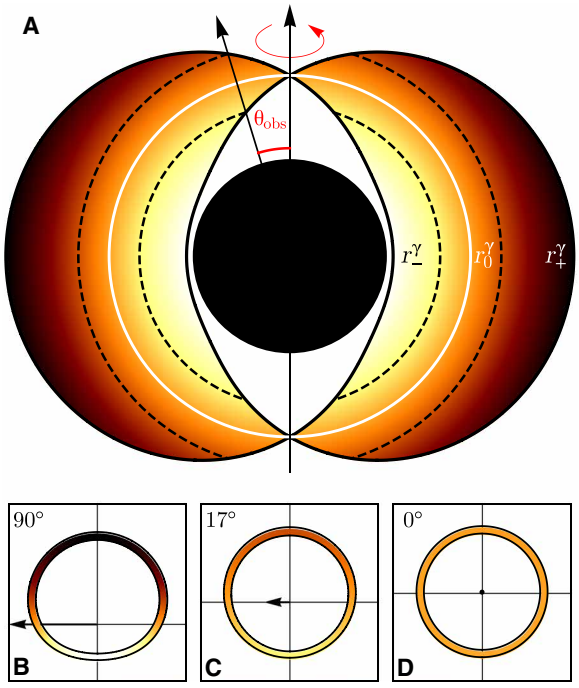

Fig. 2. Photon shell and photon ring of a Kerr black hole. (**A**) Cross section of the photon shell in the (r, θ) plane in Boyer-Lindquist coordinates. The black hole spin is $a/M = 0.94$, directed vertically, and the color varies with r. The intersection of an observer's line of sight with the photon shell boundaries at $r = r_\pm^\gamma$ determines the visible subregion of the photon shell. (**B** to **D**) Photon ring on the screen of an observer at varying inclinations θ_{obs} relative to the spin axis, whose projection onto the plane perpendicular to the line of sight is depicted by the (left-pointing) arrow. The center of the photon ring has a displacement from the origin that increases with spin. The color coding on the ring denotes the matching radius on the shell from which the photon emanated. The photon shell $r_-^\gamma \le r \le r_+^\gamma$ is only visible in its entirety to the edge-on ($\theta_{obs} = 90°$) observer. The face-on ($\theta_{obs} = 0°$) observer only receives photons from the white $r = r_0^\gamma$ orbit. The $\theta_{obs} = 17°$ observer sees the portion of the shell delineated by the dashed lines.

RESULTS

Photon shell and photon ring

This section describes the shell of unstable bound photon orbits surrounding a black hole, its lensed photon ring image, the photon subrings labeled by half-orbit number, and the angle-dependent Lyapunov exponents that govern the subring brightness ratio asymmetry. Previous treatments of these structures include (*8*) and (*10*–*13*).

Photon shell

The photon shell, illustrated in Fig. 2, is the region of a black hole spacetime containing bound null geodesics or "bound orbits" that neither escape to infinity nor fall across the event horizon. For Schwarzschild, the photon shell is the two-dimensional sphere at $r = 3M$ and any θ, ϕ, and t. For Kerr, this two-dimensional sphere fattens to a three-dimensional spherical shell. It is best described using Boyer-Lindquist coordinates, in which the metric of a Kerr black hole of mass M and angular momentum $J = aM$ (with $0 \le a \le M$) is

$$ds^2 = -\frac{\Delta}{\Sigma}(dt - a\sin^2\theta d\phi)^2 + \frac{\Sigma}{\Delta}dr^2 + \Sigma d\theta^2 + \frac{\sin^2\theta}{\Sigma}[(r^2+a^2)d\phi - a dt]^2 \quad (1A)$$

$$\Delta = r^2 - 2Mr + a^2, \quad \Sigma = r^2 + a^2\cos^2\theta \quad (1B)$$

These coordinates have the special property that each bound orbit lies at some fixed value of r in the range

$$r_-^\gamma \le r \le r_+^\gamma \quad (2A)$$

$$r_\pm^\gamma = 2M\left[1 + \cos\left(\frac{2}{3}\arccos\left(\pm\frac{a}{M}\right)\right)\right] \quad (2B)$$

Every point in the equatorial annulus $r_-^\gamma \le r \le r_+^\gamma$, $\theta = \pi/2$, has a unique bound orbit passing through it. On the boundaries $r = r_\pm^\gamma$, the orbits reside entirely in the equatorial plane. At generic points, on the other hand, they oscillate in the θ direction between polar angles

$$\theta_\pm = \arccos\left(\mp\sqrt{u_+}\right) \quad (3)$$

where

$$u_\pm = \frac{r}{a^2(r-M)^2}\left[-r^3 + 3M^2 r - 2a^2 M \pm 2\sqrt{M\Delta\left(2r^3 - 3Mr^2 + a^2 M\right)}\right] \quad (4)$$

We will refer to one such complete oscillation (e. g., from θ_- back to itself) as one orbit, since the photon typically returns to a point near, but not identical to (since the azimuthal angle ϕ also shifts), its initial position.

To summarize, the photon shell is the spacetime region

$$r_-^\gamma \le r \le r_+^\gamma, \quad \theta_- \le \theta \le \theta_+, \quad 0 \le \phi < 2\pi \tag{5}$$

(depicted in Fig. 2) for all times $-\infty \le t \le \infty$.

The bound orbit at radius r has the energy-rescaled angular momentum

$$\ell = \frac{M(r^2 - a^2) - r\Delta}{a(r - M)} \tag{6}$$

The inner circular equatorial orbit at r_-^γ is prograde, while the outer one at r_+^γ is retrograde: $\ell(r_+^\gamma) \gtrless 0$. The overall direction of the orbits reverses at the intermediate value r_0^γ for which ℓ vanishes. At that radius, $[\theta_-, \theta_+]$ equals $[0, \pi]$, and the orbits can pass over the poles.

The bound geodesics are unstable in the sense that, if perturbed slightly, they either fall into the black hole or escape to infinity where they can reach a telescope. The observed photon ring image arises from photons traveling on such "nearly bound" geodesics. Consider two geodesics, one of which is bound, with the other initially differing only by an infinitesimal radial separation δr_0. The equation of geodesic deviation shows that, after n half-orbits between $\theta_\pm$, their separation grows to

$$\delta r_n = e^{\gamma n} \delta r_0 \tag{7}$$

Here, the so-called Lyapunov exponent γ is a function on the space of bound orbits given by (see the Supplementary Materials)

$$\gamma = \frac{4}{a}\sqrt{r^2 - \frac{Mr\Delta}{(r-M)^2}} \int_0^1 \frac{dt}{\sqrt{(1-t^2)(u_+ t^2 - u_-)}} \tag{8}$$

A closely related formula appears in (*14*). Hence, the nearly bound geodesic will typically cross the equatorial plane a number of times of order

$$n \approx \frac{1}{\gamma} \ln \left| \frac{\delta r_n}{\delta r_0} \right| \tag{9}$$

until $\delta r_n \gg \delta r_0$, when the geodesic is well separated from the bound orbit and it shoots off to infinity (or crosses the event horizon if $\delta r_0 < 0$). These Lyapunov exponents are central and potentially observable quantities that characterize the geometry of the Kerr photon shell.

Photon ring and subrings

The photon ring is the image on the observer screen produced by photons on nearly bound geodesics (*7*). In the limit in which the photons become fully bound, it may be shown that their images approach a closed curve C_γ given by

$$\rho = D^{-1}\sqrt{a^2(\cos^2\theta_{obs} - u_+ u_-) + \ell^2} \tag{10A}$$

$$\varphi_\rho = \arccos\left(-\frac{\ell}{\rho\, D \sin\theta_{obs}} \right) \tag{10B}$$

where (ρ, φ_ρ) are dimensionless polar coordinates on the observer screen, while (D, θ_{obs}) denote the observer's distance and inclination from the Kerr spin axis, respectively. We can view C_γ as parameterized by the shell radius $r_-^\gamma \le r \le r_+^\gamma$ from which the photon originated. For each value of r, Eq. 10B has two solutions for φ_ρ in the range $0 \le \varphi_\rho \le 2\pi$, so each radius in the photon shell appears at two positions on C_γ. A notable consequence of Eqs. 10A and 10B is that for $\theta_{obs} \neq 0$, both ℓ and ρ, and hence φ_ρ, are functions only of r, θ_{obs}, and D. Hence, a measurement at a specific angle φ_ρ along the ring probes a specific radius r of the Kerr geometry and not, as might have been expected, a specific angle around the black hole!

Astrophysically observed photon intensities $I_{ring}(\rho, \varphi_\rho)$ at the screen can be computed by backward ray tracing. One follows the null geodesics from the observer screen back into the Kerr spacetime, integrating the Doppler-shifted strength J of matter sources along the geodesic, with attenuation factors accounting for the optical depth. Scattering effects are negligible because the expected plasma frequency and electron gyroradius are in the megahertz range, several orders of magnitude below the observing frequencies that we consider. For the images in this paper, we used ipole (*15*). A light ray aimed exactly at the curve C_γ is captured by the photon shell and (unstably) orbits the black hole forever. Those aimed inside C_γ fall into the black hole, while those aimed outside escape to infinity. Therefore, C_γ is the edge of the black hole shadow.

If we shoot a light ray very near, a distance $\delta\rho$ from the shadow edge at ρ_c, it will circle many times through the emission region before falling into the black hole or escaping to infinity. The affine length of the ray and its number of half-orbits accordingly diverge as $\delta\rho \to 0$

$$n \approx -\frac{1}{\gamma} \ln \left| \frac{\delta\rho}{\rho_c} \right| \tag{11}$$

This follows from Eq. 9 together with a computed relation between $\delta\rho$ and δr_0. For optically thin matter distributions, Eq. 11 implies a mild divergence in the observed ring intensity $I_{ring} \sim n$ as the shadow edge is approached, since a light ray that completes n half-orbits through the emission region can collect $\sim n$ times more photons along its path. The photon ring is then the bump in the photon intensity containing this logarithmic divergence at the shadow edge. Although the divergence is cut off by a finite optical depth, this notable feature remains visually prominent in many ray-traced images of GRMHD simulations, as in Fig. 1.

The photon ring can be subdivided into subrings arising from photons that have completed n half-orbits between their source and the screen. This definition for the photon ring agrees with that in (*16*) but differs from the later usage in (*9*) and (*10*) by the inclusion of the $n = 1$ and 2 contributions. These low n contributions fully account for the thin ring image visible in Fig. 1. To orbit at least $n/2$ times around the black hole, the photon must be aimed within an exponentially narrowing window

$$\frac{\delta\rho_n}{\rho_c} \approx e^{-\gamma n} \tag{12}$$

around the shadow edge. Hence, the subrings occupy a sequence of exponentially nested intervals centered around C_γ.

Each subring consists of photons lensed toward the observer screen after having been collected by the photon shell from anywhere in the universe. Hence, in an idealized setting with no absorption, each subring contains a separate, exponentially demagnified image of the entire universe, with each subsequent subring capturing the visible universe at an earlier time. Together, the set of subrings are akin to the frames of a movie, capturing the history of the visible universe as seen from the black hole. In an astrophysical setting, these images are dominated by the luminous matter around the black hole. For a black hole surrounded by a uniform distribution extending over the poles, the contributions made by each subring to the total intensity profile cannot be told apart, and the individual subrings cannot be

distinguished on the image. However, for a realistic disk or jet with emission peaked in a conical region, the subrings are visibly distinct: the nth subring is approximately a smooth peak of width $e^{-\gamma n}$. Summing these smooth peaks, like layers in a tiered wedding cake (see Fig. 3), reproduces the leading logarithmic divergence in the intensity (Eq. 11).

The photons comprising successive subrings for the same angle φ_ρ traverse essentially the same orbits and hence encounter the same matter distribution around the black hole. Apart from source variations on the time scale of an orbit, intensities of the nth and $(n+1)$th subring differ only because they correspond to windows whose widths $\delta\rho_n$ and $\delta\rho_{n+1}$ differ by a factor of $e^{-\gamma}$. Hence, for large enough n, the intensities are related by

$$I^{n+1}_{\text{ring}}(\rho_c + \delta\rho, \varphi_\rho) \approx I^{n}_{\text{ring}}(\rho_c + e^{\gamma}\delta\rho, \varphi_\rho) \tag{13}$$

We therefore find the angle-dependent subring flux ratio

$$\frac{F^{n+1}_{\text{ring}}}{F^{n}_{\text{ring}}} \approx e^{-\gamma} \tag{14}$$

Equations 13 and 14 are matter-independent predictions for the photon ring structure that involve only general relativity. The prediction holds only for "large enough" n: At small n, there are nonuniversal matter-dependent effects from photons that do not traverse exactly the same region around the black hole. Insight into when n is large enough might be obtained from GRMHD simulations.

Since the exponent γ depends on a, θ_{obs}, and φ_ρ (see the Supplementary Materials), the flux ratio asymmetry in Eq. 14 provides a new method for determination of the spin. For Schwarzschild, $\gamma = \pi$ (*8*), corresponding to a demagnification factor of $e^{-\pi} \approx 4\%$. For a black hole of maximal spin $a/M = 1$ viewed from an inclination $\theta_{\text{obs}} = 17^\circ$ [as estimated for M87; (*17*)], the factor $e^{-\gamma}$ is as large as 13% on the part of the ring where the black hole spins toward the observer. Although Eq. 12 breaks down for $n = 0$, this suppression factor suggests that the leading $n = 1$ subring should provide ~10% of the total luminosity, in order-of-magnitude agreement with GRMHD simulations.

Interferometric signatures of a photon ring

This section explores the response of an interferometer to the photon ring through a series of increasingly refined geometrical models. We first review the interferometric signatures of an infinitesimally thin, uniform, and circular ring. We then extend this treatment to include rings with nonuniform brightness, nonzero thickness, and noncircular structure. We conclude this section by discussing specific features expected for the photon ring and its subrings.

Visibilities for a thin, uniform, and circular ring

Each baseline joining two elements of an interferometer samples a complex visibility $V(\mathbf{u})$, which corresponds to a single Fourier component of the sky image $I(\mathbf{x})$ (*18*)

$$V(\mathbf{u}) = \int I(\mathbf{x})\, e^{-2\pi i \mathbf{u}\cdot\mathbf{x}}\, \mathrm{d}^2\mathbf{x} \tag{15}$$

Here, $\mathbf{u}$ is the dimensionless vector baseline projected orthogonal to the line of sight and measured in units of the observation wavelength λ, while $\mathbf{x}$ is a dimensionless image coordinate measured in radians.

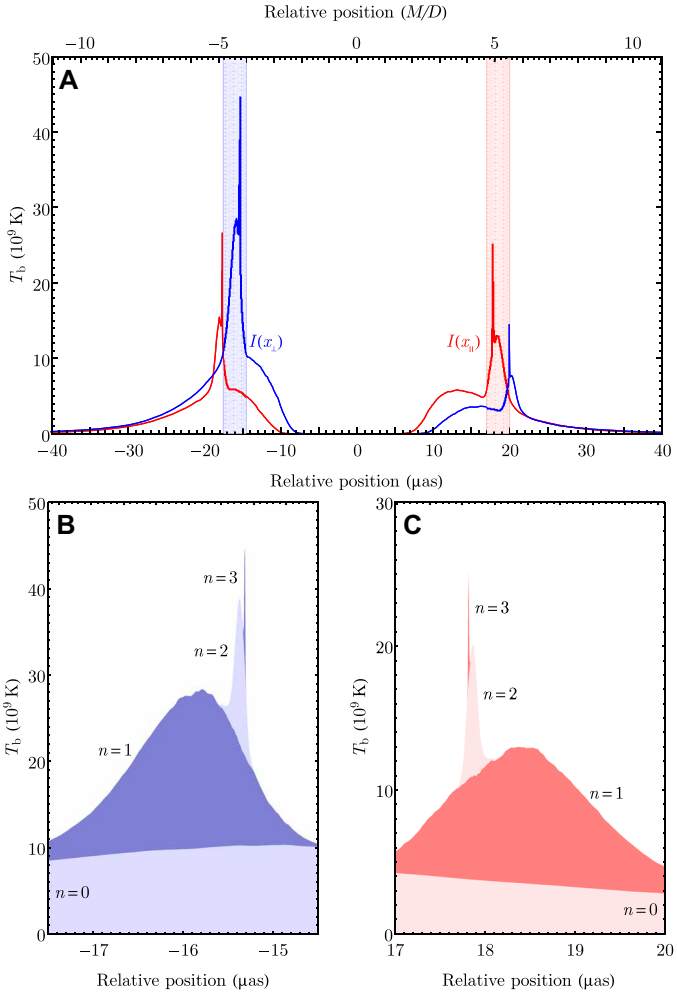

Fig. 3. Image cross sections of a photon ring and its subrings. (**A**) Brightness cross sections for the time-averaged GRMHD image shown in Fig. 1. The blue/red curves show cross sections perpendicular/parallel to the projected spin axis. (**B** and **C**) Decomposition of the left perpendicular peak and the right parallel peak into subrings indexed by the number n of photon half-orbits executed between turning points (Eq. 3) in the polar motion. Similar results are also seen in image cross sections of simple geometrical models (*10*).

In terms of polar coordinates (ρ, φ_ρ) on the observer screen (Eqs. 10A and 10B), the image and corresponding visibility function of an infinitesimally thin, uniform, and circular ring are

$$I(\rho, \varphi_\rho) = \frac{1}{\pi d}\delta\left(\rho - \frac{d}{2}\right) \tag{16A}$$

$$V(u, \varphi_u) = J_0(\pi d u) \tag{16B}$$

where d is the ring diameter in radians and the image is normalized to have a total flux density of unity, $V(0) = 1$. J_m denotes the mth Bessel function of the first kind, which admits the asymptotic expansion

$$J_m(\pi d u) \approx \frac{1}{\pi}\sqrt{\frac{2}{du}}\cos\left[\pi\left(du - \frac{2m+1}{4}\right)\right] \tag{17}$$

valid for $\pi d u \gg m^2$. Hence, $V(u)$ is a weakly damped pure frequency with period $\Delta u = 2/d$ inside an envelope that falls as $1/\sqrt{u}$.

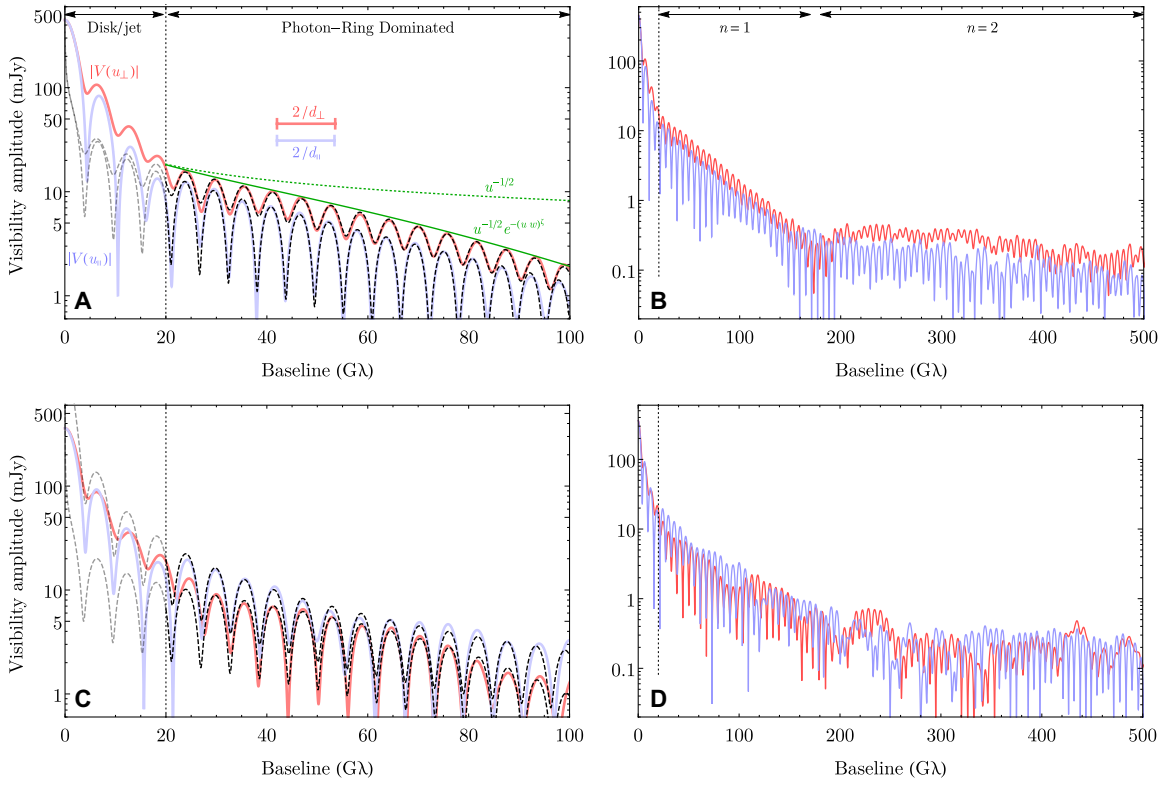

Fig. 4. Universal interferometric signatures of a photon ring. (**A** to **D**) Visibility amplitudes of (A and B) the time-averaged GRMHD simulation shown in Fig. 1 and (C and D) a GRMHD snapshot (see the Supplementary Materials). Amplitudes are shown for baselines perpendicular (red) and parallel (blue) to the black hole spin axis. While short baselines (left of the vertical dotted lines) display complex structure reflecting astrophysical features of the image such as emission from the disk and jet, longer baselines are dominated by the universal interferometric signatures of the photon ring. A simple model $|V(u)| = |\alpha_+ \cos(\pi du) + \alpha_- \sin(\pi du)|\,(du)^{-1/2}e^{-(wu)^\zeta}$ is overplotted (black dashed curves), with parameters determined independently along the two axes. The periodicities encode the ring diameters along each axis and hence *M*/*D* for the black hole; their difference provides an estimate of the black hole spin and inclination. The parameters $\alpha_\pm$ carry information about the angular brightness distribution (and hence spin and inclination). The dashed green curve $u^{-1/2}$ shows the expected envelope for an infinitesimally thin ring, while the solid green curve $u^{-1/2}e^{-(wu)^\zeta}$ shows the fitted envelope that carries information about the ring thickness. On even longer baselines (B and D), the dominant visibility contributions arise from subrings with increasingly higher *n*. The universal features are more prominent in the time-averaged image, whose ring is dominated by smaller mode numbers *m* and which has less small-scale power outside the photon ring.

Visibilities for a nonuniform ring

The image of a thin ring with nonuniform brightness in φ_ρ decomposes into a sum over angular Fourier modes

$$I(\rho,\varphi_\rho) = \frac{1}{\pi d}\delta\left(\rho - \frac{d}{2}\right)\sum_{m=-\infty}^{\infty}\beta_m e^{im\varphi_\rho} \tag{18}$$

where $\beta_{-m} = \beta_m^*$ since the image is real. The total image flux density is given by $\beta_0 > 0$.

The corresponding visibility function is

$$V(u,\varphi_u) = \sum_{m=-\infty}^{\infty}\beta_m J_m(\pi du)\, e^{im(\varphi_u-\pi/2)} \tag{19}$$

Using Eq. 17, for long baselines, we may approximate

$$V(u,\varphi_u) \approx \frac{\alpha_+(\varphi_u)\cos(\pi du) + \alpha_-(\varphi_u)\sin(\pi du)}{\sqrt{du}}$$
$$\alpha_\pm(\varphi_u) \equiv \frac{1}{\pi}\sum_{m=-\infty}^{\infty}\beta_m e^{im\left[\varphi_u + \frac{\pi}{2}(m-1\pm1)\right]} \tag{20}$$

Thus, for sufficiently long baselines, the radial visibility function of a nonuniform thin ring is determined by a single pair of weakly damped, orthogonal modes $\alpha_\pm(\varphi_u)$. Their envelope still fall as $|V(u)| \sim 1/\sqrt{u}$, and the modes have a common period of $\Delta u = 2/d$ in complex visibilities (or $\Delta u = 1/d$ in visibility amplitudes). The angular spectrum of the image $\{\beta_m\}$ is easily retrieved from the angular spectrum of the visibilities (see the Supplementary Materials).

Visibilities for a thick ring

Baselines of length $u \gtrsim 1/L$ are required to resolve image features of size $\lesssim L$. Hence, the visibility function of any ring with diameter d and thickness $w \ll d$ has two asymptotic regimes

$$(\mathrm{I}):\frac{1}{d} \ll u \ll \frac{1}{w}, \qquad (\mathrm{II}):\frac{1}{d} \ll \frac{1}{w} \ll u \tag{21}$$

Baselines in regime (I) resolve the diameter of the ring but not its thickness, while longer baselines in regime (II) resolve both. Hence, the visibility function in regime (I) behaves like that of a thin ring (a damped periodicity with envelope $|V(u)| \sim 1/\sqrt{u}$), while the envelope of the visibility function in regime (II) is sensitive to the radial profile of the ring. In general, the visibility of any smooth ring decays exponentially in regime (II), although images with discontinuous derivatives, such as a uniform disk or annulus, can have slower, power-law falloffs.

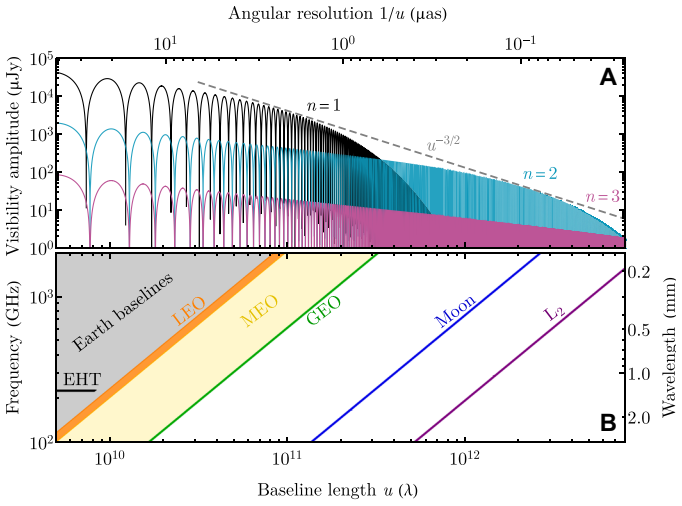

Fig. 5. Prospects for observing a photon ring. (**A**) Schematic showing visibility amplitude as a function of baseline length for a photon ring with $d = 40$ μas and flux density comparable to M87. The black, cyan, and magenta visibilities correspond to photons with half-orbit numbers $n = 1$, 2, and 3. (**B**) Frequency-dependent range of Earth baselines and representative Earth-space baselines. Earth-space baselines shown are the longest baselines for an orbiter in low Earth orbit (LEO), in medium Earth orbit (MEO), in geostationary orbit (GEO), on the Moon, and at the second Sun-Earth Lagrange point (L_2).

The validity of the approximation of Eq. 17 in regime (I) depends on the amount of power at high values of m. Specifically, it requires $m_{\max} \lesssim \sqrt{\pi d/w}$. Under this condition, $|V(u)|$ has $\lesssim d/w$ periods in regime (I).

Visibilities for a noncircular ring

Although the photon ring is nearly circular for all black hole spins and inclinations, the primary interferometric signatures discussed thus far do not require an image with perfectly circular structure. For instance, if an image is stretched, $I(x, y) \to I'(x, y) = I(ax, by)$; then, its visibility function is correspondingly compressed, $V(u, v) \to V'(u, v) = |ab|^{-1} V(u/a, v/b)$. Thus, the visibility profiles of a stretched ring share the properties and asymptotic expansions derived for a circular ring (e. g., Eq. 20), except that the radial periodicities become a function of position angle. To leading order in the asymmetry $1 - a/b$, the diameter corresponding to a damped radial periodicity in the visibility domain matches that of the stretched ring along the baseline's position angle. For the black hole in M87, the asymmetry is expected to be a few percent at most, even for a maximally rotating black hole (see fig. S2).

Visibilities of the photon subrings

As discussed earlier, the photon ring decomposes into subrings labeled by the photon half-orbit number n. According to Eq. 14, the width of the radial intensity profile produced by the nth subring is $w_n \sim w_0 e^{-\gamma n}$, while the brightness remains approximately constant with n (until some $n_{\max}$ determined by the optical depth). Each subring thus contributes a periodically modulated visibility, $V_n(u) \sim w_n/\sqrt{u}$, which falls more steeply for baselines $u > 1/w_n$. Hence, the nth subring dominates the signal in the regime

$$\frac{1}{w_{n-1}} \ll u \ll \frac{1}{w_n} \tag{22}$$

This implies that the totality of subring contributions has an envelope defined by this turnover behavior

$$V(u) \approx \sum_{\substack{n \\ w_n < 1/u}} \frac{w_n}{\sqrt{u}} \sim \frac{1}{u^{3/2}} \tag{23}$$

Together, the subrings then form a cascade of damped oscillations on progressively longer baselines, each dominated by the image of a single subring and conveying precise information about its diameter, thickness, and angular profile. Figure 4 displays visibilities of the time-averaged GRMHD image in Fig. 1, which exhibit the expected damped periodicity, as well as clear contributions on long baselines from distinct subrings (see Fig. 5 for a schematic illustration of this cascade).

DISCUSSION

Detection of the photon ring's universal interferometric signatures requires measurements on longer baselines, with finer angular resolution than those currently available to the EHT. This extension can be achieved either by observing at higher frequencies or on longer physical baselines via space VLBI. For reference, ALMA (Atacama Large Millimeter/submillimeter Array) currently observes up to 950 GHz (ALMA band 10) with higher frequencies (up to 1.53 THz) possible in the future (*19*, *20*). Figure 5 shows baseline lengths for a variety of array configurations and observing frequencies.

For the EHT to observe the photon ring, it must also achieve sufficient sensitivity to detect its visibilities. For both Sgr A* and M87, the horizon-scale emission has a total flux density of $F_{\rm tot} \sim 1$ Jy at $\lambda \sim 1$ mm (*21*, *22*), with a fraction $f_{\rm ring} \sim 10\%$ expected to come from the photon ring. The expected amplitude of the photon ring on long interferometric baselines is thus

$$|V(\mathbf{u})| \sim 30 \text{ mJy} \left(\frac{|\mathbf{u}|}{10 \text{ G}\lambda}\right)^{-3/2} \left(\frac{d}{40 \text{ μas}}\right)^{-1/2} \left(\frac{f_{\rm ring}}{0.1}\right) \left(\frac{F_{\rm tot}}{1 \text{ Jy}}\right) \tag{24}$$

For comparison, a baseline from ALMA to a 4-m orbiter with 32 GHz of averaged bandwidth and a 10-min coherent integration would have a thermal noise of $\sigma_{950} \approx 3$ mJy at 950 GHz and $\sigma_{690} \approx 1.3$ mJy at 690 GHz. For baselines from ALMA to a 10-m orbiter, such as the proposed Millimetron mission for L_2 (*23*, *24*), the thermal noise would be $\sigma_{950} \approx 1$ mJy and $\sigma_{690} \approx 0.5$ mJy. Another possibility would be to place a VLBI station on or orbiting the Moon, which could sample many periods of the $n = 2$ regime of M87 at current EHT observing frequencies. A 10-m dish on the Moon could achieve $\sigma \approx 0.1$ mJy on baselines to ALMA with coherent integrations of 10 min and a bandwidth of 32 GHz.

These sensitivities could be substantially improved via simultaneous multifrequency observations. In addition to having more sensitive receivers and longer coherence times, lower frequencies give correspondingly shorter baselines and thus increased interferometric power from the photon ring. Phase calibration with lower frequencies could then allow substantially longer integration times at higher frequencies (see the Supplementary Materials for additional details and discussion).

Interferometric signatures of the photon ring are most prominent when the image has little small-scale power outside the ring and when the ring has a smooth angular profile dominated by low mode numbers m. Both of these conditions are met in time-averaged images of black hole accretion flows, such as in Fig. 1. Because visibilities of a time-averaged image are equal to time-averaged visibilities of a variable image, developing capabilities for long, coherent averaging could significantly improve the prospects for unambiguous detection and characterization of the photon ring.

In summary, precise measurements of the size, shape, thickness, and angular profile of the nth photon subring of M87 and Sgr A* may be feasible for $n = 1$ using a high-frequency ground array or low Earth orbits, for $n = 2$ with a station on the Moon and for $n = 3$ with a station in L_2.

SUPPLEMENTARY MATERIALS

Supplementary material for this article is available at http://advances.sciencemag.org/cgi/content/full/6/12/eaaz1310/DC1

Supplementary Materials and Methods

Fig. S1. Lyapunov exponent as a function of image angle.

Fig. S2. Black hole shadow diameter and asymmetry as a function of spin and inclination.

Fig. S3. Snapshot images and visibilities.

References (*25*–*34*)

REFERENCES AND NOTES

1. Event Horizon Telescope Collaboration, K. Akiyama, A. Alberdi, W. Alef, K. Asada, R. Azulay, A.-K. Baczko, D. Ball, M. Baloković, J. Barrett, D. Bintley, L. Blackburn, W. Boland, K. L. Bouman, G. C. Bower, M. Bremer, C. D. Brinkerink, R. Brissenden, S. Britzen, A. E. Broderick, D. Broguiere, T. Bronzwaer, D.-Y. Byun, J. E. Carlstrom, A. Chael, C.-k. Chan, S. Chatterjee, K. Chatterjee, M.-T. Chen, Y. Chen, I. Cho, P. Christian, J. E. Conway, J. M. Cordes, G. B. Crew, Y. Cui, J. Davelaar, M. De Laurentis, R. Deane, J. Dempsey, G. Desvignes, J. Dexter, S. S. Doeleman, R. P. Eatough, H. Falcke, V. L. Fish, E. Fomalont, R. Fraga-Encinas, W. T. Freeman, P. Friberg, C. M. Fromm, J. L. Gómez, P. Galison, C. F. Gammie, R. García, O. Gentaz, B. Georgiev, C. Goddi, R. Gold, M. Gu, M. Gurwell, K. Hada, M. H. Hecht, R. Hesper, L. C. Ho, P. Ho, M. Honma, C.-W. L. Huang, L. Huang, D. H. Hughes, S. Ikeda, M. Inoue, S. Issaoun, D. J. James, B. T. Jannuzi, M. Janssen, B. Jeter, W. Jiang, M. D. Johnson, S. Jorstad, T. Jung, M. Karami, R. Karuppusamy, T. Kawashima, G. K. Keating, M. Kettenis, J.-Y. Kim, J. Kim, J. Kim, M. Kino, J. Y. Koay, P. M. Koch, S. Koyama, M. Kramer, C. Kramer, T. P. Krichbaum, C.-Y. Kuo, T. R. Lauer, S.-S. Lee, Y.-R. Li, Z. Li, M. Lindqvist, K. Liu, E. Liuzzo, W.-P. Lo, A. P. Lobanov, L. Loinard, C. Lonsdale, R.-S. Lu, N. R. MacDonald, J. Mao, S. Markoff, D. P. Marrone, A. P. Marscher, I. Martí-Vidal, S. Matsushita, L. D. Matthews, L. Medeiros, K. M. Menten, Y. Mizuno, I. Mizuno, J. M. Moran, K. Moriyama, M. Moscibrodzka, C. Müller, H. Nagai, N. M. Nagar, M. Nakamura, R. Narayan, G. Narayanan, I. Natarajan, R. Neri, C. Ni, A. Noutsos, H. Okino, H. Olivares, G. N. Ortiz-León, T. Oyama, F. Özel, D. C. M. Palumbo, N. Patel, U.-L. Pen, D. W. Pesce, V. Piétu, R. Plambeck, A. PopStefanija, O. Porth, B. Prather, J. A. Preciado-López, D. Psaltis, H.-Y. Pu, V. Ramakrishnan, R. Rao, M. G. Rawlings, A. W. Raymond, L. Rezzolla, B. Ripperda, F. Roelofs, A. Rogers, E. Ros, M. Rose, A. Roshanineshat, H. Rottmann, A. L. Roy, C. Ruszczyk, B. R. Ryan, K. L. J. Rygl, S. Sánchez, D. Sánchez-Arguelles, M. Sasada, T. Savolainen, F. P. Schloerb, K.-F. Schuster, L. Shao, Z. Shen, D. Small, B. W. Sohn, J. SooHoo, F. Tazaki, P. Tiede, R. P. J. Tilanus, M. Titus, K. Toma, P. Torne, T. Trent, S. Trippe, S. Tsuda, I. van Bemmel, H. J. van Langevelde, D. R. van Rossum, J. Wagner, J. Wardle, J. Weintroub, N. Wex, R. Wharton, M. Wielgus, G. N. Wong, Q. Wu, K. Young, A. Young, Z. Younsi, F. Yuan, Y.-F. Yuan, J. Anton Zensus, G. Zhao, S.-S. Zhao, Z. Zhu, J.-C. Algaba, A. Allardi, R. Amestica, J. Anczarski, U. Bach, F. K. Baganoff, C. Beaudoin, B. A. Benson, R. Berthold, J. M. Blanchard, R. Blundell, S. Bustamente, R. Cappallo, E. Castillo-Domínguez, C.-C. Chang, S.-H. Chang, S.-C. Chang, C.-C. Chen, R. Chilson, T. C. Chuter, R. C. Rosado, I. M. Coulson, T. M. Crawford, J. Crowley, J. David, M. Derome, M. Dexter, S. Dornbusch, K. A. Dudevoir, S. A. Dzib, A. Eckart, C. Eckert, N. R. Erickson, W. B. Everett, A. Faber, J. R. Farah, V. Fath, T. W. Folkers, D. C. Forbes, R. Freund, A. I. Gómez-Ruiz, D. M. Gale, F. Gao, G. Geertsema, D. A. Graham, C. H. Greer, R. Grosslein, F. Gueth, D. Haggard, N. W. Halverson, C.-C. Han, K.-C. Han, J. Hao, Y. Hasegawa, J. W. Henning, A. Hernández-Gómez, R. Herrero-Illana, S. Heyminck, A. Hirota, J. Hoge, Y.-D. Huang, C. M. Violette Impellizzeri, H. Jiang, A. Kamble, R. Keisler, K. Kimura, Y. Kono, D. Kubo, J. Kuroda, R. Lacasse, R. A. Laing, E. M. Leitch, C.-T. Li, L. C.-C. Lin, C.-T. Liu, K.-Y. Liu, L.-M. Lu, R. G. Marson, P. L. Martin-Cocher, K. D. Massingill, C. Matulonis, M. P. McColl, S. R. McWhirter, H. Messias, Z. Meyer-Zhao, D. Michalik, A. Montaña, W. Montgomerie, M. Mora-Klein, D. Muders, A. Nadolski, S. Navarro, J. Neilsen, C. H. Nguyen, H. Nishioka, T. Norton, M. A. Nowak, G. Nystrom, H. Ogawa, P. Oshiro, T. Oyama, H. Parsons, S. N. Paine, J. Peñalver, N. M. Phillips, M. Poirier, N. Pradel, R. A. Primiani, P. A. Raffin, A. S. Rahlin, G. Reiland, C. Risacher, I. Ruiz, A. F. Sáez-Madaín, R. Sassella, P. Schellart, P. Shaw, K. M. Silva, H. Shiokawa, D. R. Smith, W. Snow, K. Souccar, D. Sousa, T. K. Sridharan, R. Srinivasan, W. Stahm, A. A. Stark, K. Story, S. T. Timmer, L. Vertatschitsch, C. Walther, T.-S. Wei, N. Whitehorn, A. R. Whitney, D. P. Woody, J. G. A. Wouterloot, M. Wright, P. Yamaguchi, C.-Y. Yu, M. Zeballos, S. Zhang, L. Ziurys, First M87 event horizon telescope results. I. The shadow of the supermassive black hole. *Astrophys. J. Lett.* **875**, L1 (2019).
2. Event Horizon Telescope Collaboration, First M87 event horizon telescope results. II. Array and instrumentation. *Astrophys. J. Lett.* **875**, L2 (2019).
3. Event Horizon Telescope Collaboration, First M87 event horizon telescope results. III. Data processing and calibration. *Astrophys. J. Lett.* **875**, L3 (2019).
4. Event Horizon Telescope Collaboration, First M87 event horizon telescope results. IV. Imaging the central supermassive black hole. *Astrophys. J. Lett.* **875**, L4 (2019).
5. Event Horizon Telescope Collaboration, First M87 event horizon telescope results. V. Physical origin of the asymmetric ring. *Astrophys. J. Lett.* **875**, L5 (2019).
6. Event Horizon Telescope Collaboration, First M87 event horizon telescope results. VI. The shadow and mass of the central black hole. *Astrophys. J. Lett.* **875**, L6 (2019).
7. J. M. Bardeen, Timelike and null geodesics in the Kerr metric, in *Black Holes (Les Astres Occlus)*, C. DeWitt, B. S. DeWitt, Eds. (Gordon and Breach, 1973), pp. 215–239.
8. J.-P. Luminet, Image of a spherical black hole with thin accretion disk. *Astron. Astrophys.* **75**, 228–235 (1979).
9. T. Johannsen, D. Psaltis, Testing the no-hair theorem with observations in the electromagnetic spectrum. II. Black hole images. *Astrophys. J.* **718**, 446 (2010).
10. S. E. Gralla, D. E. Holz, R. M. Wald, Black hole shadows, photon rings, and lensing rings. *Phys. Rev. D* **100**, 024018 (2019).
11. C. Darwin, The gravity field of a particle. *Proc. R. Soc. Lond. Ser. A* **249**, 180 (1959).
12. J. M. Bardeen, W. H. Press, S. A. Teukolsky, Rotating black holes: Locally nonrotating frames, energy extraction, and scalar synchrotron radiation. *Astrophys. J.* **178**, 347–370 (1972).
13. E. Teo, Spherical photon orbits around a kerr black hole. *Gen. Relativ. Gravit.* **35**, 1909–1926 (2003).
14. H. Yang, D. A. Nichols, F. Zhang, A. Zimmerman, Z. Zhang, Y. Chen, Quasinormal-mode spectrum of Kerr black holes and its geometric interpretation. *Phys. Rev. D* **86**, 104006 (2012).
15. M. Mościbrodzka, C. F. Gammie, IPOLE—Semi-analytic scheme for relativistic polarized radiative transport. *Mon Not. R. Astron. Soc.* **475**, 43–54 (2018).
16. K. Beckwith, C. Done, Extreme gravitational lensing near rotating black holes. *Mon. Not. R. Astron. Soc.* **359**, 1217–1228 (2005).
17. R. C. Walker, P. E. Hardee, F. B. Davies, C. Ly, W. Junor, The structure and dynamics of the subparsec jet in M87 based on 50 VLBA observations over 17 years at 43 GHz. *Astrophys. J.* **855**, 128 (2018).
18. A. R. Thompson, J. M. Moran, J. Swenson, W. George Jr., *Interferometry and Synthesis in Radio Astronomy* (Springer, ed. 3, 2017).
19. M. C. Wiedner, F. Bielau, M. Emprechtinger, K. Rettenbacher, N.-H. Volgenau, G. Wieching, U.-U. Graf, C.-E. Honningh, K. Jacobs, R. Guesten, K.-M. Menten, S. Philipp, D. Rabanus, R. Simon, J. Stutzki, F. Wyrowsk, Observations at THz frequencies with CONDOR, in *Molecules in Space and Laboratory*, J. L. Lemaire, F. Combes, Eds. (2007), pp. 16.
20. D. Rigopoulou, R. Laing, S. Withington, G. Magdis, S. Graves, J. Richer, B. Ellison, Report on the Workshop "Science with ALMA Band 11 (1.0-1.6 THz)". *Messenger* **153**, 35–37 (2013).
21. G. C. Bower, S. Markoff, J. Dexter, M. A. Gurwell, J. M. Moran, A. Brunthaler, H. Falcke, P. C. Fragile, D. Maitra, D. Marrone, A. Peck, A. Rushton, M. C. H. Wright, Radio and millimeter monitoring of Sgr A*: Spectrum, variability, and constraints on the G2 encounter. *Astrophys. J.* **802**, 69 (2015).
22. A. Chael, R. Narayan, M. D. Johnson, Two-temperature, Magnetically Arrested Disc simulations of the jet from the supermassive black hole in M87. *Mon. Not. R. Astron. Soc.* **486**, 2873–2895 (2019).
23. W. Wild, N. S. Kardashev; On behalf of the Millimetron consortium, S. F. Likhachev, N. G. Babakin, V. Y. Arkhipov, I. S. Vinogradov, V. V. Andreyanov, S. D. Fedorchuk, N. V. Myshonkova, Y. A. Alexsandrov, I. D. Novokov, G. N. Goltsman, A. M. Cherepaschuk, B. M. Shustov, A. N. Vystavkin, V. P. Koshelets, V. F. Vdovin, T. de Graauw, F. Helmich, F. vd Tak, R. Shipman, A. Baryshev, J. R. Gao, P. Khosropanah, P. Roelfsema, P. Barthel, M. Spaans, M. Mendez, T. Klapwijk, F. Israel, M. Hogerheijde, P. vd Werf, J. Cernicharo, J. Martin-Pintado, P. Planesas, J. D. Gallego, G. Beaudin, J. M. Krieg, M. Gerin, L. Pagani, P. Saraceno, A. M. Di Giorgio, R. Cerulli, R. Orfei, L. Spinoglio, L. Piazzo, R. Liseau, V. Belitsky, S. Cherednichenko, A. Poglitsch, W. Raab, R. Guesten, B. Klein, J. Stutzki, N. Honingh, A. Benz, A. Murphy, N. Trappe, A. Räisänen, Millimetron—A large Russian-European submillimeter space observatory. *Exp. Astron.* **23**, 221–244 (2009).
24. N. S. Kardashev, I. D. Novikov, V. N. Lukash, S. V. Pilipenko, E. V. Mikheeva, D. V. Bisikalo, D. S. Wiebe, A. G. Doroshkevich, A. V. Zasov, I. I. Zinchenko, P. B. Ivanov, V. I. Kostenko, T. I. Larchenkova, S. F. Likhachev, I. F. Malov, V. M. Malofeev, A. S. Pozanenko, A. V. Smirnov, A. M. Sobolev, A. M. Cherepashchuk, Y. A. Shchekinov, Review of scientific topics for the Millimetron space observatory. *Physics Uspekhi* **57**, 1199–1228 (2014).
25. D. Kapec, A. Lupsasca, Particle motion near high-spin black holes, (2019); arXiv:1905.11406
26. F. Mertens, A. P. Lobanov, R. C. Walker, P. E. Hardee, Kinematics of the jet in M 87 on scales of 100–1000 Schwarzschild radii. *Astron. Astrophys.* **595**, A54 (2016).
27. C.-k. Chan, D. Psaltis, F. Özel, GRay: A massively parallel GPU-based code for ray tracing in relativistic spacetimes. *Asrophys. J.* **777**, 13 (2013).
28. B. S. Robinson, D. M. Boroson, C. M. Schieler, F. I. Khatri, O. Guldner, S. Constantine, T. Shih, J. W. Burnside, B. C. Bilyeu, F. Hakimi, A. Garg, G. Allen, E. Clements, D. M. Cornwell, TeraByte InfraRed Delivery (TBIRD): A demonstration of large-volume direct-to-earth data transfer from low-earth orbit, in *Free-Space Laser Communication and Atmospheric Propagation XXX*, (SPIE, 2018), vol. 10524, pp. 105240V.

29. S. Doeleman, T. Mai, A. E. E. Rogers, J. G. Hartnett, M. E. Tobar, N. Nand, Adapting a cryogenic sapphire oscillator for very long baseline interferometry. *Publ. Astron. Soc. Pac.* **123**, 582 (2011).
30. A. E. Broderick, A. Loeb, M. J. Reid, Localizing sagittarius A* and M87 on microarcsecond scales with millimeter very long baseline interferometry. *Astrophys. J.* **735**, 57 (2011).
31. E. Middelberg, A. L. Roy, R. C. Walker, H. Falcke, VLBI observations of weak sources using fast frequency switching. *Astron. Astrophys.* **433**, 897–909 (2005).
32. M. Rioja, R. Dodson, High-precision astrometric millimeter very long baseline interferometry using a new method for atmospheric calibration. *Astron. J.* **141**, 114 (2011).
33. M. J. Rioja, R. Dodson, T. Jung, B. W. Sohn, The power of simultaneous multifrequency observations for mm-VLBI: Astrometry up to 130 GHz with the KVN. *Astron. J.* **150**, 202 (2015).
34. Z. Zhu, M. D. Johnson, R. Narayan, Testing general relativity with the black hole shadow size and asymmetry of sagittarius A*: Limitations from interstellar scattering. *Astrophys. J.* **870**, 6 (2019).

Acknowledgments: We thank A. Broderick, Z. Frankel, J. Goldfield, S. Gralla, E. Himwich, H.-Y. Pu, and Z. Younsi. **Funding:** This work was supported by the National Science Foundation (AST-1440254, AST-1716536, AST-1716327, OISE-1743747, and PHY-1205550), the Gordon and Betty Moore Foundation (GBMF-5278), the Department of Energy (DE-SC000998), (DE-SC0007870 to A.S.), NASA (no. HST-HF2-51431.001-A), and the Black Hole Initiative at Harvard University through a grant (60477) from the John Templeton Foundation. **Author contributions:** M.D.J., A.L., A.S., S.H., R.N., A.C., P.G., and D.C.M.P. formulated the ideas in this paper in discussions on the theoretical aspects of the photon shell and ring. S.H., D.K., A.L., and A.S. developed the treatment of Lyapunov exponents that characterize the instability of bound photon orbits and determine the angle-dependent subring brightness ratios. M.D.J. conceived the idea of distinctive interferometric signatures of these subrings and derived the initial expressions for them. G.N.W. adapted the IPOLE software to enable high-resolution images and to provide the subring decomposition from the ray tracing, as well as provided the high-cadence GRMHD fluid simulations. M.D.J. and A.L. wrote the original draft. A.S., G.N.W., D.K., S.H., R.N., P.G., and D.C.M.P. provided significant text and contributions. All authors contributed to review and editing. **Competing interests:** The authors declare that they have no competing interests. **Data and materials availability:** All data needed to evaluate the conclusions in the paper are present in the paper and/or the Supplementary Materials. Additional data related to this paper may be requested from the authors.

Submitted 14 August 2019
Accepted 19 December 2019
Published 18 March 2020
10.1126/sciadv.aaz1310

Citation: M. D. Johnson, A. Lupsasca, A. Strominger, G. N. Wong, S. Hadar, D. Kapec, R. Narayan, A. Chael, C. F. Gammie, P. Galison, D. C. M. Palumbo, S. S. Doeleman, L. Blackburn, M. Wielgus, D. W. Pesce, J. R. Farah, J. M. Moran, Universal interferometric signatures of a black hole's photon ring. *Sci. Adv.* **6**, eaaz1310 (2020).